ROYAL SOCIETY OF CHEMISTRY

PAPER

Check for updates

Twist-angle programmable magnetism in graphene/CrI₃ bilayers

Florentino López-Urías [a] and Francisco Sánchez-Ochoa [*b]

A graphene monolayer lacks an electronic bandgap and magnetism, which limits its application as components in electronic and spintronic devices. Proximity effects in graphene with other two-dimensional (2D) materials are a promising route to induce properties in van der Waals (vdW) heterostructures. Here, we build twisted vdW graphene/CrI₃ heterostructures and then study their electronic and magnetic properties using collinear spin-polarized density functional theory (DFT) calculations. Four twisted heterostructures were built with maximal biaxial strain to avoid renormalization of the band structures and possible expansion, shrinkage, or corrugation of the monolayers. We found the same electronic bandwidth in graphene with an induced magnetism by the ferromagnetic and semiconducting CrI₃ monolayer substrate. Fingerprints of moiré effects are observed in the calculated local spin density, spin-polarization ratio, orbital-resolved density of states, and unfolded band structures of graphene. Besides the twist-angle dependent Zeeman splitting found in graphene, we obtained an enhancement of magnetic exchange coupling in CrI₃. These results show that the interlayer rotation angle is an additional degree of freedom to compression and electric fields for programming magnetism density in graphene as well as in the CrI₃ monolayer.

1 Introduction

With the miniaturization of technology and the increase in transistors per unit area of processors on the nanoscale, the community has focused on sheet-like materials, known as two-dimensional (2D) materials. In particular, 2D layered materials are promising candidates for nanoelectronic applications. Graphene (G) is the most studied 2D layered material because of its successful experimental realization *via* mechanical exfoliation.[1] G is an atomically thin sheet of carbon atoms. Although a free-standing G monolayer is a non-magnetic semimetal with a zero-bandgap, the G system is considered to be the workhorse in the 2D material realm, similar to bulk silicon in the traditional electronic industry. It is noteworthy that spintronics is an alternative to traditional electronics that deals with electron charge,[2] because it takes advantage of the electron spin to transfer information and data storage applications with lower power consumption.[3] In the last decade, one of the most significant advancements in 2D spintronics has been the experimental realization of anisotropic semiconducting 2D magnets made of CrI₃, questioning the Mermin–Wagner theorem for the realization of 2D magnetism.[4] The experimental synthesis of 2D single-layer magnets has inspired investigations to understand their novel physics and identify their unexplored applications.[5,6]

Novel 2D magnetic heterostructure materials can be created by stacking G with semiconducting ferromagnets, such as CrI₃ layers, through weak vdW interactions. These systems exhibit intriguing phenomena because of the coexistence of graphene's high electron mobility and long spin relaxation lengths,[7] and the magnetic properties of the ferromagnetic (FM) and semiconducting layers, making them promising for spintronic[8,9] and valleytronic device applications.[10] Moreover, this G/CrI₃ heterostructure is considered a quantum platform candidate for the theoretical study of Wigner states,[11] Chern insulator states under compression, and anomalous Hall effects.[12,13] In this G/CrI₃ heterostructure, the magnetic proximity effect (MPE) strongly depends on the interlayer electronic hybridization between the layers.[14] Experimentally, the G layer has been employed to probe the magnetic and insulating CrI₃ electronic structure through scanning tunneling microscopy/spectroscopy (STM/STS) measurements.[15] There are gate-dependent transport properties in G induced by the MPE of CrI₃ layers, without evidence of a magnetic exchange field in G.[16] Other layered magnetic materials such as Cr₂Ge₂Te₆[17] and CrB₃[18,19] have been employed to induce MPEs on G as a Zeeman splitting field in G.[18] In contrast, the G adsorbed onto the (001) surface

[a] *División de Materiales Avanzados, Instituto Potosino de Investigación Científica y Tecnológica, Camino a la Presa San José 2055, Col. Lomas 4a Sección, San Luis Potosí, S.L.P 78216, Mexico*

[b] *Departamento de Materia Condensada, Instituto de Física, Universidad Nacional Autónoma de México, Apartado Postal 20-364, Ciudad de México C.P. 01000, Mexico*

of $Co_3Sn_2S_2$ shows an enhancement in the perpendicular magnetic anisotropy energy of each system, with promising applications in magnetic recording devices.[20] Europium (with strong spin–orbit coupling (SOC)) doping on single-layer G supported by the Co(0001) surface is employed to generate single spin-polarized bands close to the Fermi energy (at the M-point) and the bandgap formation of the n-doped Dirac point (at the K-point), as revealed by spin- and angle-resolved photoemission spectroscopy (ARPES) experiments.[21] Finally, in addition to the interlayer compression (external pressure) and electric field (gate voltage) degrees of freedom to enhance MPEs in G/CrI_3 heterostructures,[8,10,13,15,22] the inclusion of relative orientation (defined by the interlayer angle θ) to control the exchange splitting and SOC in G is an interesting topic.[17,23]

Herein, we present the electronic and magnetic properties of G induced by CrI_3 monolayers with different θ values. The results show clear evidence of θ-dependent moiré effects in the magnetized G in real space, in the density of states (DOS), in the spin-polarization ratio (SPR), and in electronic band structures with the formation of magnetic minigaps in G, and a twistable Zemman band splitting in the Dirac cones of G. This twist-angle programmable Zemman splitting in G is similar to that found in G/CrI_3 systems under compression[22] and in the $G/Cr_2Ge_2Te_6$ system for different θ values.[17] Furthermore, we observe that the magnetic exchange between the Cr atoms was enhanced by G. The outline of this paper is as follows: the computational density functional theory (DFT) methodology is presented in Section 2, results and discussion are presented in Section 3, and conclusions are presented in Section 4.

2 Computational methodology

Owing to the large number of atoms in the heterostructures and the lack of relativistic effects on the norm-conserving Troullier–Martins pseudopotentials employed to treat electron–ion interactions,[24] the spin–orbit coupling (SOC) effect was not addressed, and only collinear spin-polarized DFT calculations were performed using the SIESTA code (version master-4.1).[25,26] The lack of a relativistic effect in pseudopotentials prevents the inclusion of the SOC term within this SIESTA version.[27] A vdW exchange–correlation functional with Vydrov and Van Voorhis (VV) parameterization was used.[28] Because the SIESTA code uses a linear combination of numerical pseudoatomic orbitals (LCAO), we employed an extended double-ζ polarized (DZP) basis set to expand the Kohn–Sham wavefunctions and an energy mesh-cutoff of 500 Ry for sampling the electronic density in real space. The radial extension of atomic orbitals was controlled by the single parameter PAO.EnergyShift of 50 meV plus a PAO.SplitNorm of 0.15 for the generation of the secondary and polarizable orbitals. Moreover, effective Hubbard U_{eff} ($U_{eff} = U - J$) corrections (DFT+U),[29] to address the on-site Coulomb interactions for Cr(3d) orbitals, are absent for simplicity. This is because there is no consensus for U_{eff} values, which can achieve values greater than 6 eV,

depending on the numerical approach.[30–33] The lattice vectors and atomic positions were well-converged using a $15 \times 15 \times 1$ Monkhorst–Pack k grid[34] for the smallest G/CrI_3 heterostructure with $\theta = 30.0°$. An electronic temperature of 10 K was used for Fermi surface broadening. The lattice vectors and atomic positions were optimized until the residual forces were 5 meV/Å or less, while the threshold value for electronic self-consistency was 10^{-4} eV. We employed the supercell (SC) method with a vacuum space of 20 Å to avoid artificial interactions between replicas. Dipole corrections were included to compensate for the electric dipole generated by the G/CrI_3 slab and obtain correct band offsets.[35] Atomic models and charge/spin isosurfaces were visualized using VESTA.[36]

# 3 Results

3.1 Structural parameters

The left panels in Fig. 1 show the top view of G and CrI_3 unit cells sharing the same hexagonal Bravais lattice. On an atomic basis, the G monolayer has two carbon atoms, whereas the CrI_3 monolayer has two Cr and six I atoms, forming edge-sharing octahedra. We optimized the whole structures (atomic positions and lattice vectors) and obtained the lattice constants of $a_G = 2.45$ Å and $a_{CrI_3} = 7.07$ Å. The calculated lattice constants, a_G and a_{CrI_3}, are in fair agreement with those reported for G[37,38] and CrI_3[12,39] monolayers. As a reference, the zigzag directions were extended parallel to the lattice vectors of both the G (carbon zigzag lines) and CrI_3 (polyhedral zigzag lines) unit cells. Using the optimized unit cells, we employed the Nookiin software[40] to build the four smallest commensurable G/CrI_3 heterostructures, as shown in Fig. 1. Constraints of $m \geq n$ and $p \geq q$ were used to generate systems with θ values within the 0–30° range. In addition, the Nookiin software generated the integer pairs, (m,n) for G and (p,q) for CrI_3, as shown in the first and third rows of Table 1. These sets of integers pairs are useful to define the corresponding transformation matrix for each hexagonal monolayer, P_G and P_{CrI_3}:

$$P_G(m,n) = \begin{pmatrix} m & n \\ -n & m+n \end{pmatrix},$$
$$P_{CrI_3}(p,q) = \begin{pmatrix} p & q \\ -q & p+q \end{pmatrix}. \tag{1}$$

Besides, the integers m, n, p, and q were used for calculating the relative interlayer rotation angle (θ), the biaxial strain (Δ) on G, and the total number of atoms (N_t) in the twisted G/CrI_3 heterostructures by:[41,42]

$$\theta = \cos^{-1}\left[\frac{m \cdot p + n \cdot q + (m \cdot q + n \cdot p/2)}{\sqrt{m^2 + n^2 + m \cdot n} \times \sqrt{p^2 + q^2 + p \cdot q}}\right] \times \left(\frac{180°}{\pi}\right), \tag{2}$$
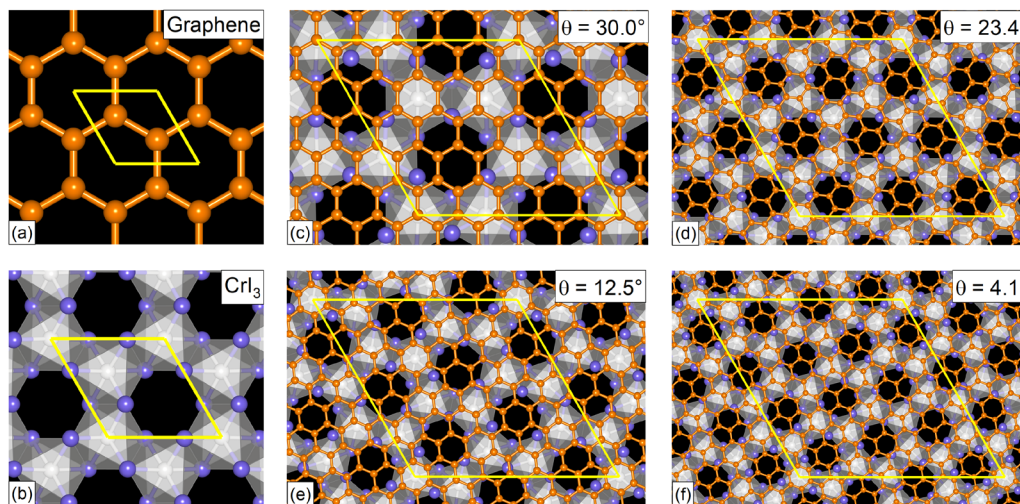
Fig. 1 Atomic models of (a) G (ball-and-stick) and (b) CrI$_3$ (gray polyhedra) monolayers, and twisted magnetic heterostructures composed of G and CrI$_3$ layers with (c) 30.0°, (d) 23.4°, (e) 12.5° and (f) 4.1°. C, Cr, and I atoms are presented in orange, silver, and purple colors. The yellow lines delimit the periodic cell.

$$\Delta = \frac{a_G\sqrt{m^2 + n^2 + m \cdot n} - a_{CrI_3}\sqrt{p^2 + q^2 + p \cdot q}}{a_{CrI_3}\sqrt{p^2 + q^2 + p \cdot q}} \times 100\%, \quad (3)$$

$$N_t = 2(m^2 + n^2 + m\cdot n) + 8(p^2 + q^2 + p\cdot q). \quad (4)$$

The calculated θ, Δ, and N_t values are presented in Table 1. As in previous reports, Fig. 1 shows that as the θ value decreases, the N_t value increases, or the moiré SC size also increases. For example, for the system with $\theta = 30.0°$, a direct inspection shows that along the carbon zigzag lines of G, there are parallel armchair polyhedral lines from the CrI$_3$ layer. The maximum θ value was 30° with an initial small expansion of $\Delta = +0.04\%$ on the G layer and $N_t = 74$ atoms in the entire heterostructure. In contrast to the previous system, at $\theta = 4.1°$, the heterostructure has $N_t = 310$ atoms, and the G layer undergoes an initial shrinkage effect of $\Delta = -2.45\%$. Let us mention that, since all the integer pairs are different from zero, except (5,0) for G and (3,0) for CrI$_3$, the 2D transformation

matrices defined in eqn (1) involve two symmetry operations on the monolayers, expansion and rotation, and we can define a general notation for lattice periodicity (reconstruction), as in the second and fourth rows of Table 1. Thus, the lattice periodicities of 5×5 for G and 3×3 for CrI$_3$ involve only an expansion along the lattice vectors; see the systems with $\theta = 30.0°$ and $23.5°$ in comparison with the initial unit cell structures in Fig. 1. Additionally, the SC lattice constant can be calculated as the periodicity factor multiplied by the primitive lattice constant. For example, when $\theta = 4.1°$, $a_G^{SC} = a_G\sqrt{|\det P_G(9,2)|} = a_G\sqrt{103}$ and $a_{CrI_3}^{SC} = a_{CrI_3}\sqrt{|\det P_{CrI_3}(3,1)|} = a_{CrI_3}\sqrt{13}$ due to the hexagonal lattice symmetry of the SC.[43] More data can be found in Table SI of the Supplementary Information (SI) for systems in which, despite the higher (m,n) and (p,q) integers, the θ values fall within the 19–28° range.

3.2 Electronic structure of pristine monolayers

The ground state electronic structure of G and CrI$_3$ single layers are depicted in Fig. 2. The electronic band structure of G shows

Table 1 (m,n) and (p,q) integers to construct hexagonal commensurable SCs of G and CrI$_3$. Integers pairs allow to define a G- and CrI$_3$-periodicity. θ is the interlayer rotation angle (eqn (2)) in degrees, Δ is the biaxial strain (eqn (3)) percentage, and N_T is the total number of atoms in the SC (eqn (4)). The (k_x,k_y) values of the equivalent K_G and M_G high-symmetry points of the G primitive cell (PC) in the reciprocal space of the heterostructure are reported. The total energy difference between the FM and AFM states, ΔE_{FM-AFM}, is reported in meV per CrI$_3$ unit cell. The exchange parameter value J is reported in meV per Cr ion

$(m,n)_G$	(5,0)	(6,4)	(7,1)	(9,2)
G-periodicity	5×5	$2\sqrt{19} \times 2\sqrt{19}$	$\sqrt{3 \cdot 19} \times \sqrt{3 \cdot 19}$	$\sqrt{103} \times \sqrt{103}$
$(p,q)_{CrI_3}$	(1,1)	(3,0)	(2,1)	(3,1)
CrI$_3$-periodicity	$\sqrt{3} \times \sqrt{3}$	3×3	$\sqrt{7} \times \sqrt{7}$	$\sqrt{13} \times \sqrt{13}$
θ	30.0	23.4	12.5	4.1
Δ	+0.04	+0.70	−1.11	−2.45
N_T	74	224	170	310
$K_G(k_x,k_y)$	5/3,5/3	2/3,14/3	2,3	7/3,13/3
$M_G(k_x,k_y)$	5/2,0	3,2	7/2,1/2	9/2,1
ΔE_{FM-AFM}	−85	−77	−87	−67
J	−3.15	−2.85	−3.22	−2.48

an already known linear dispersion around the *K* point at the Fermi energy owing to C(2p$_z$) orbitals. Within this numerical DFT calculation, we found a hopping parameter $t_{pp\pi} \sim 2.4$ eV for C(2p$_z$)–C(2p$_z$) orbital interactions, giving a π-band which extends from 0 to ~ -7.2 eV, see Fig. S1(a) of the SI. The σ-bands composed of C(2s) and C(2p$_{x,y}$) orbitals start from ~ -3.5 eV and extend towards deeper energy values in the valence regime. The total density of states (DOS) of G shows a null value at 0 eV (Fermi energy), which is characteristic of the Dirac point in the band structure. In Fig. S1(b) of the SI, the total DOS increases linearly around 0 eV, with two van Hove singularities near −2 eV and −6.5 eV owing to the π-band and σ-bands, respectively.

In contrast to the non-magnetic G layer, the CrI$_3$ monolayer is a FM semiconductor with a single-spin narrow band gap by the majority-spin states around the Fermi energy. The calculated majority-spin direct band gap was ~ 1 eV positioned at the Γ point. The obtained bandgap value is similar to 0.82 or 0.89 (1.19 or 1.23) eV in ref. 12 and 44, with Hubbard parametrization within the generalized gradient approximation with (without) the SOC term. Less dispersive electronic bands along the fully scanned *k*-path resemble the ionic bonding properties of an insulator. The hexagonal crystalline structure of the CrI$_3$ monolayer has a point symmetry D_{3d}. The crystal field induced by the I atoms splits with the Cr(3d) levels in an orbital triplet t$_{2g}$ and a higher energy doublet e$_g$. Hence, the Cr(3d) levels of the Cr^{3+} ions should be occupied by three electrons, which occupy the single spin t$_{2g}$ triplet to minimize both orbital energy and Coulomb repulsion. However, the

reported average magnetic moment $>4\mu_B$ in Table SIII (SI) is overestimated with the Mulliken charges in Table SII of the SI. Regarding the spin-resolved total DOS, the single unoccupied majority-spin states above the Fermi energy are a mixture of Cr(3d) and I(5p) orbitals,[44] which, in our case, are separated from other single unoccupied minority-spin states at approximately 4 eV.

3.3 Spin-polarized graphene

In this section, we discuss the collinear magnetism induced on G by the CrI$_3$ monolayer through the MPE. Once the ground state is achieved using the self-consistent method within SIESTA, we numerically calculate the local spin density $\sigma(r)$ as follows[45]:

$$\sigma(r) = \rho_\uparrow(r) - \rho_\downarrow(r), \tag{5}$$

where $\rho_\uparrow(r)$ ($\rho_\downarrow(r)$) denotes the total majority-spin (minority-spin) charge density. Fig. 3 shows the four G/CrI$_3$ heterostructures with a translucent plane positioned at the interface between the two layers to visualize only the minority-spin contributions located on the carbon atoms. Here, the unbalanced charge in C(2p$_z$) orbitals allows a localized spin density. Note that, as θ decreases, the coverage of carbon atoms with local minority-spin contribution also decreases, as shown in Fig. 3. A high coverage of localized magnetic moments on carbon atoms was observed for high θ values. Several FM carbon pairs or triads are observed at $\theta = 30.0°$, although only FM dimers are present with a few FM triads and some single FM atoms at $\theta = 4.1°$. Tables SII and SIII in the SI show numerical values of total charge, Mulliken charges, and magnetic moments per cell and atom. Additionally, Fig. S2 in the SI shows the 2D spatial distribution of magnetic moments in G monolayers. Thus, a moiré-like induced collinear spin-polarized effect is observed in G in the real space. We expect these results to motivate experimentalists to study these G/CrI$_3$ heterostructures to visualize single spin-polarized moiré states in G.[15,21]

Second, we plot the partial DOS per spin for each heterostructure in the top panels of Fig. 4. After full optimization of the four G/CrI$_3$ heterostructures, we found that the C(2p$_z$) orbitals retain an electronic bandwidth of ~ -7.2 eV. The 2D quantum confinement of G can be observed from −7 eV to −5 eV with equal contributions from both spins. Furthermore, an asymmetric and oscillatory behavior is observed from −5 eV to 0.5 eV. As can be seen, linear dispersion is kept for minority-spin states above the Fermi energy and around the Dirac point, while the majority-spin states undergo energy broadening and enhancement induced by the CrI$_3$ layer. Regarding the van Hove singularity positioned at −2 eV, attenuation plus a small energy spin-splitting is achieved as θ decreases. To enhance the effect of θ on the spin-polarized electronic states in G, we calculated the spin-polarization ratio (SPR),[45] also known as the spin-filtering efficiency (SFE), using the results of the partial DOS shown in the top panels of Fig. 4. The SPR is calculated as
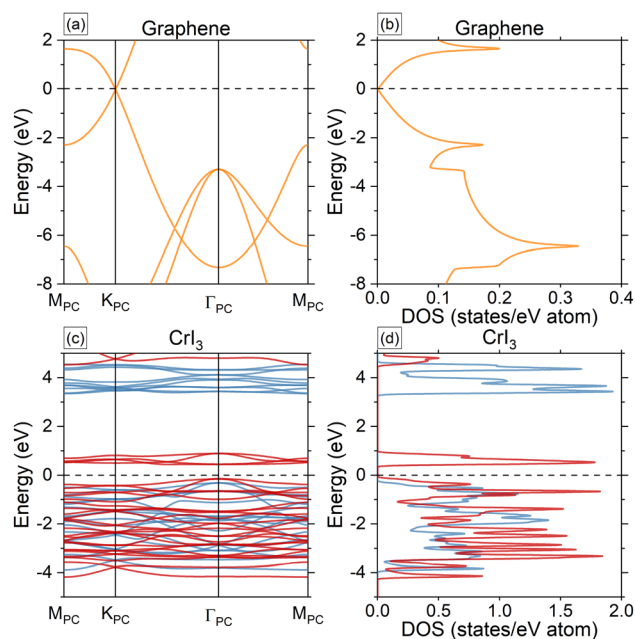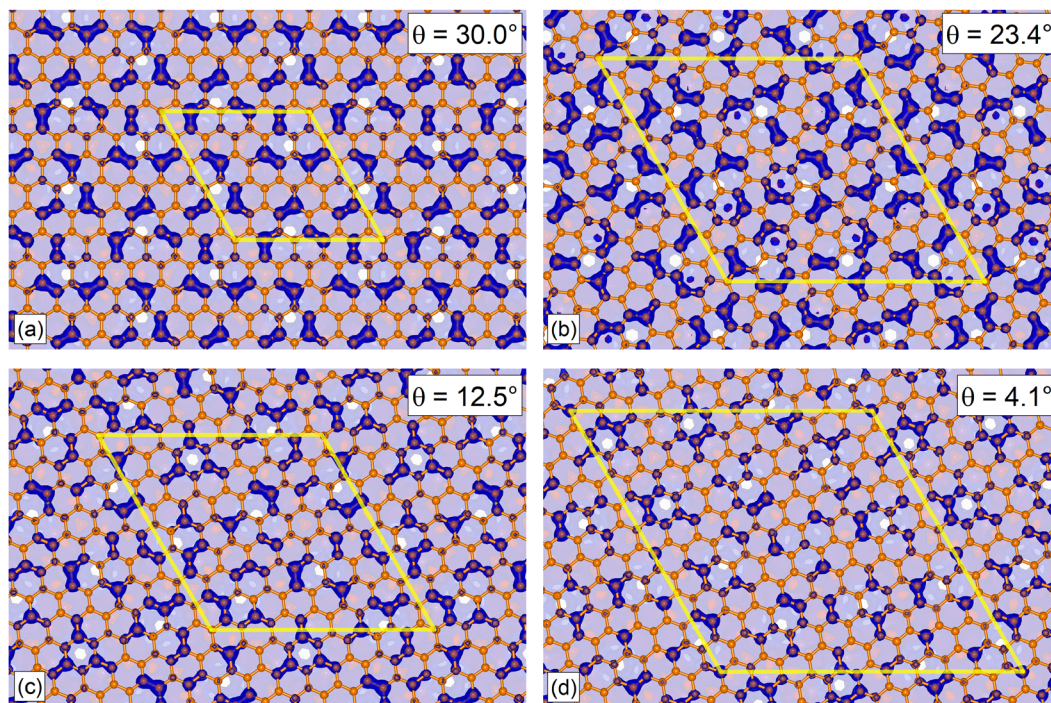

Fig. 2 Band structures along the directions connecting the high-symmetry points for non-magnetic (a) G and (c) FM CrI$_3$ primitive cells and their corresponding normalized DOS in (b) G and (d) CrI$_3$. The Fermi energy is set to 0 eV. For CrI$_3$, the majority-spin and minority-spin contributions are colored with red and blue, respectively.

Fig. 3 Calculated local spin density in twisted G/CrI$_3$ heterostructures with interlayer angles of (a) 30.0°, (b) 23.4°, (c) 12.5° and (d) 4.1°, where the yellow line denotes the periodic supercell. The blue color means minority-spin contributions in carbon atoms. Carbon atoms without a blue isosurface have an almost null local magnetization.
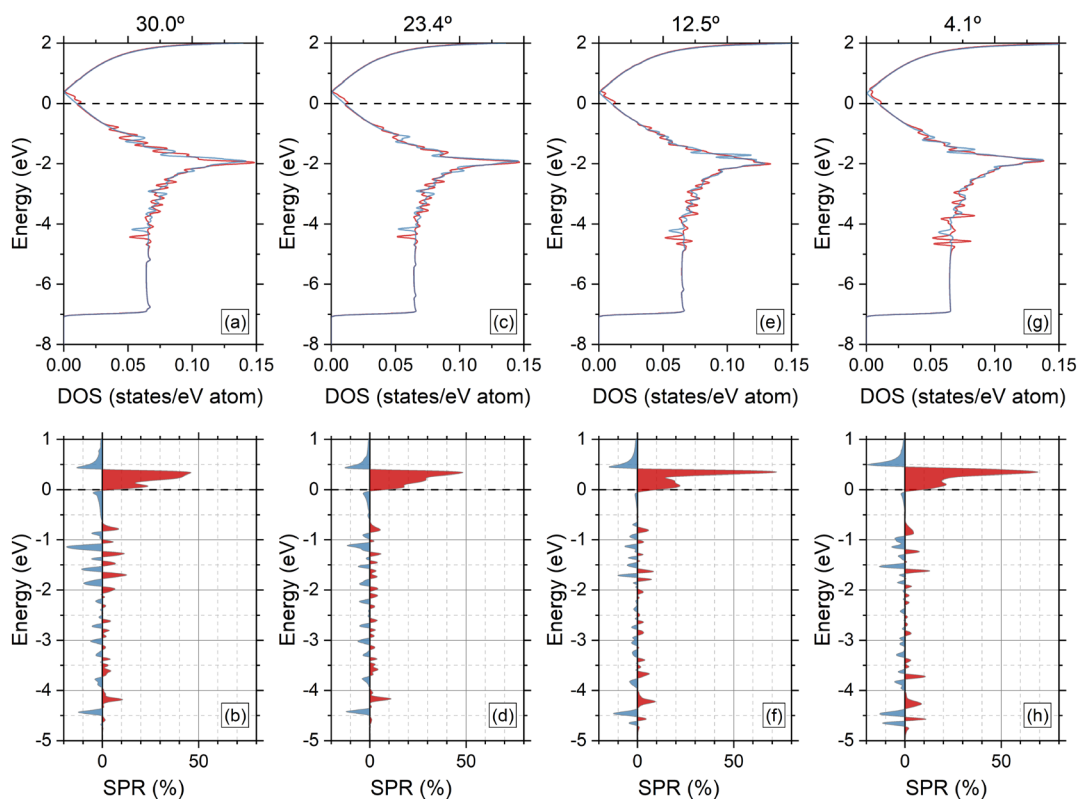
Fig. 4 Top panel: (a), (c), (e) and (g) show the average spin-polarized DOS for G C(2p$_z$) orbitals. Red (blue) curves represent majority-spin (minority-spin) contributions. Bottom panel: (b), (d), (f) and (h) show the corresponding spin-polarization ratio (SPR), with positive (negative) values labeling majority-spin (minority-spin) contributions. In both panels, the Fermi energy is set to 0 eV.

follows:

$$\text{SPR} = \frac{\text{DOS}_\uparrow[\text{C}(2\text{p}_z)] - \text{DOS}_\downarrow[\text{C}(2\text{p}_z)]}{\text{DOS}_\uparrow[\text{C}(2\text{p}_z)] + \text{DOS}_\downarrow[\text{C}(2\text{p}_z)]} \times 100\%, \quad (6)$$

where $\text{DOS}_\uparrow[\text{C}(2\text{p}_z)]$ and $\text{DOS}_\downarrow[\text{C}(2\text{p}_z)]$ are the orbital-resolved DOS with majority-spin and minority-spin contributions, respectively. The SPR results are shown in the bottom panels of Fig. 4. The moiré effect on the magnetic states of G can be observed mainly from -5 eV to 1 eV. Around the Fermi energy, electronic G states with majority-spin contributions tend to increase as θ decreases, which is a positive SPR value, showing a narrow peak that not only increases from 45% to 70% but also has an up-shift in energy. From 0.5 to 1 eV and from 0 to -0.5 eV, we found regions with single-spin polarized states with minority-spin contributions. Also, note that a moiré effect is observed for unoccupied minority-spin states around 0.5 eV, plus an increase in the SPR of 10%. The complex oscillatory behavior in the SPR for energies lower than -1 eV is a clear fingerprint of the moiré effect in G/CrI$_3$ heterostructures. To end this section, we found SPR values on average less than 10% which slightly extended towards deep energies. This is shown for SPR values around -4.5 eV, as shown in Fig. 4.

3.4 Supercell band structure

In this subsection, we discuss the results of the SCs electronic band structures. Because the four G/CrI$_3$ heterostructures maintain the hexagonal symmetry, we employed the following relative (or fractional) coordinates for the high-symmetry points in the irreducible SC Brillouin zone: $\gamma_{\text{SC}} = (0,0)$, $k_{\text{SC}} = (1/3,1/3)$, and $m_{\text{SC}} = (0,1/2)$. The band structures per spin are shown in Fig. 5. In general, as the SC size or number of atoms increases, the SC system shrinks in reciprocal space, showing that several electronic states merge into the SC (mini) Brillouin zone, which is smaller than that of the original G or CrI$_3$ PCs. This is due to the so-called 'band-folding' process of the electronic states.[42] The folding mechanism usually provides a challenging interpretation of the physical results. In addition, this standard SC band structure result is not directly comparable to angle-resolved photoelectron spectroscopy (ARPES) measurements. Despite this, in this subsection, we focus on a small energy window around the Fermi energy to show that the low dispersive first conduction energy bands probably from the CrI$_3$ monolayer are positioned just at the Fermi level. This indicates electron doping by charge transfer from the G layer, which is hole-doped. To observe the electron deficit in the G layer, we present a 2D plot of the atomic charges in the carbon atoms in Fig. S3 of the SI. However, in the energy window in Fig. 5, the CrI$_3$ majority-spin contributions are mixed with those of the G monolayer, whereas the G minority-spin contributions remain non-perturbed. As in previous reports,[37,41,46] whenever the SC G monolayer has a $3n$ total number of atoms, the high symmetry points K_G and K'_G of the G PC fold to the center of the SC
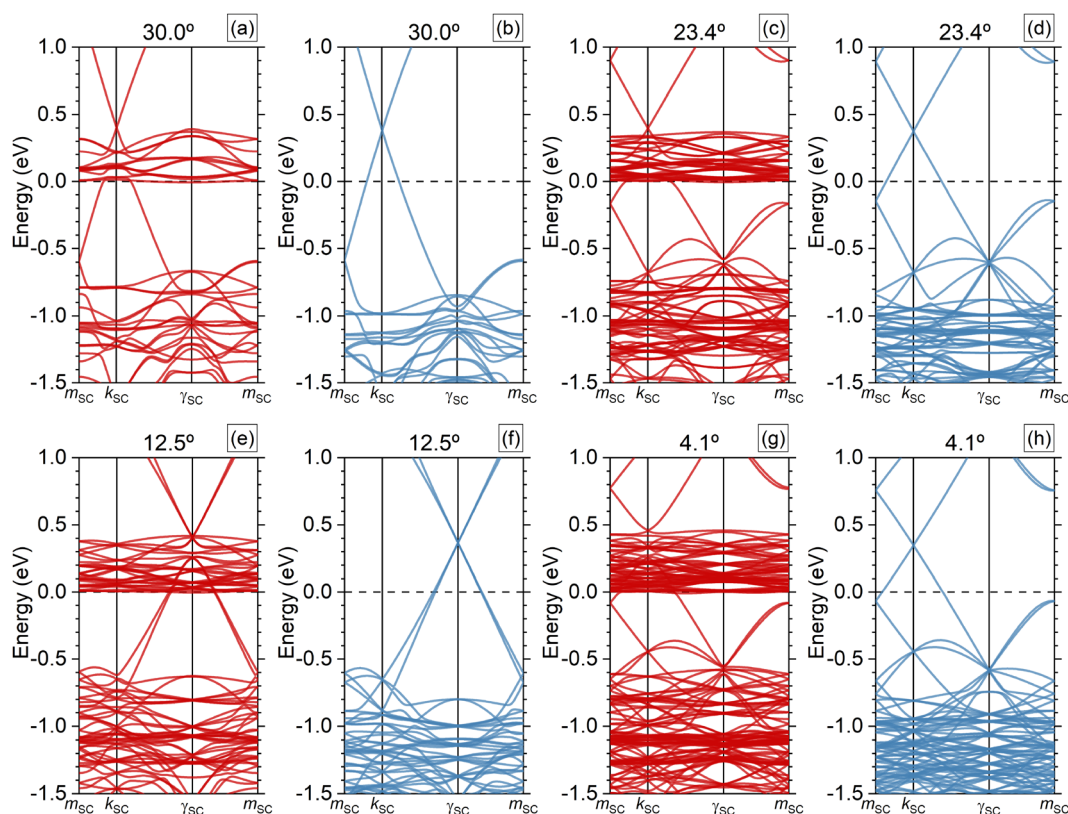

Fig. 5 Calculated supercell (SC) band structures of magnetic heterostructures with collinear spin-polarized states in (a), (c), (e) and (g) colored with red for majority-spin states, while in (b), (d), (f) and (h) with blue for minority-spin states. m_{SC}, k_{SC}, and γ_{SC} are the high-symmetry points defining the irreducible SC (mini) Brillouin zone. The Fermi energy is set to 0 eV.

Brillouin zone. In other words, the (K_G, K'_G)-points map towards the γ-point of the SC Brillouin zone. Hence, the band folding of $(K_G, K'_G) \rightarrow \gamma_{SC}$ is present in the G monolayer only for the G/CrI$_3$ heterostructure with θ = 12.5° for both spin contributions. This is because the determinant of the matrix transformation, $|\det P_G(7,1)|$ = 57 = 3 × 19, gives an integer number of three, whereas the other three G supercells probably have the next mapping, $(K_G, K'_G) \rightarrow (k_{SC}, k'_{SC})$ Additionally, it is worth mentioning that for θ = 12.5°, the two hole-doped and degenerate linear bands around the Dirac point have contributions from the K_G and K'_G valleys from the G PC. And, at first sight, the G states close to Dirac points with the majority-spin states, red color in Fig. 5, hybridized directly with the CrI$_3$ states at θ = 12.5° and 4.1°, whereas the other two systems with high θ = 30.0° and 23.4° did not.

3.5 Magnetic minigaps in graphene

In this section, we present the results of the spin-resolved unfolding method for periodic SCs in order to obtain an effective band structure per spin. Based on the stated computational methodology, the present results solely consider collinear spin interactions. This means that the Hamiltonian has

the following form:

$$H = \begin{pmatrix} H_{\uparrow\uparrow} & 0 \\ 0 & H_{\downarrow\downarrow} \end{pmatrix}, \quad (7)$$

with the electron density for the majority $\rho(r)_\uparrow$ and minority $\rho(r)_\downarrow$ giving the total electronic density $\rho(r) = \rho(r)_\uparrow + \rho(r)_\downarrow$ and the spin density in eqn (5). This allows Hamiltonian and electron decoupling, from which the spectral weight, $W^I(k)$,[38,42] can be calculated separately for each spin contribution. Thus, by using the formalism described in ref. 42, we can define for each I-th band the majority-spin contributions as:

$$W^I_\uparrow(k) = \frac{1}{N} \sum_{u \varepsilon PC} \left[\sum_j^N c^{I,(u+j)*}_\uparrow(k) \right] \times \left[\sum_j^N c^{I,(u+j)}_\uparrow(k) \right], \quad (8)$$

where the symbol $\uparrow$ represents the majority-spin states. The same $W^I_\downarrow(k)$ quantity can be defined for the minority-spin contributions. Here, the j labels all basis orbitals in space, while the I label is for different bands, and $c^I_\uparrow(k)$ corresponds to the complex coefficients from the Kohn–Sham orbitals obtained self-consistently taking collinear spins. Once the $W^I_\uparrow(k)$ calculation was performed, the results were deconvoluted
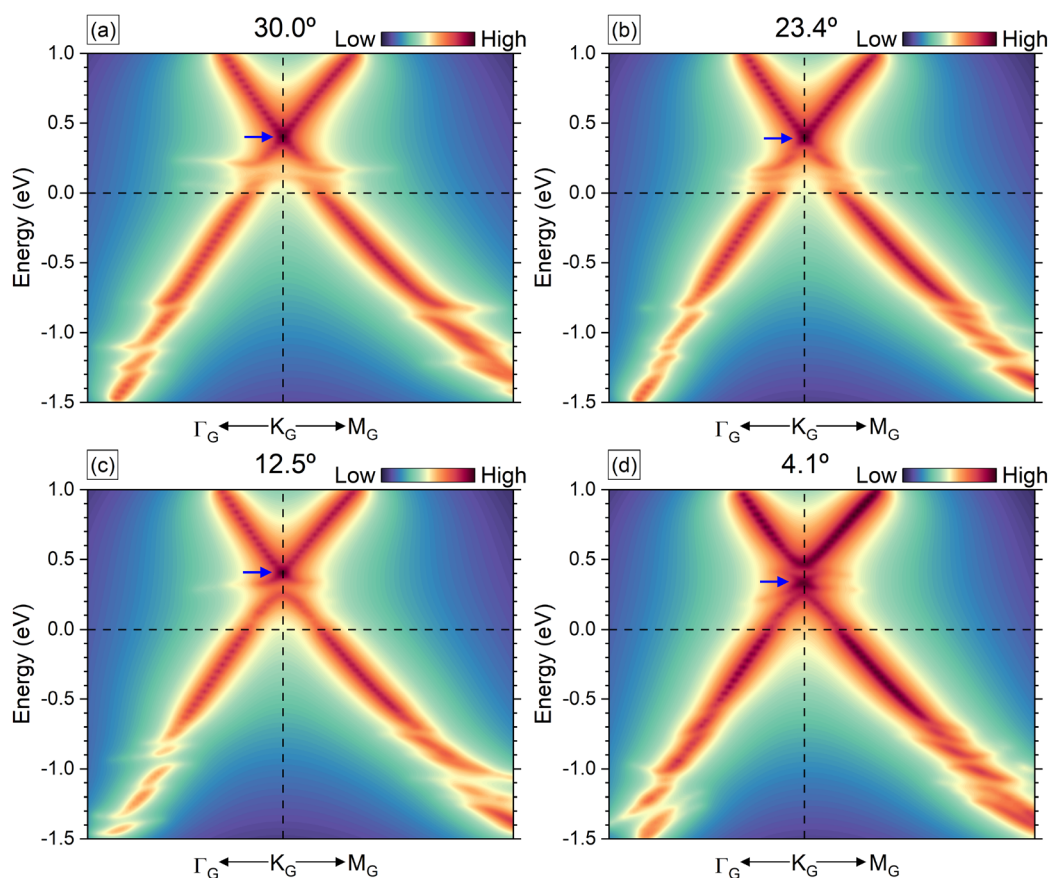
Fig. 6 Effective band structures projected onto the G PC with (a) 30.0°, (b) 23.4°, (c) 12.5° and (d) 4.1°. Only the majority–spin contributions around the K_G point are plotted. The spectral weight, $W^I_\uparrow(k)$, is calculated for every electronic state. The dashed horizontal black line at 0 eV represents the Fermi energy. Blue arrows indicate the position of Dirac point.

using the following Lorentzian function:

$$CH_4N_2O \xrightarrow{550\,°C} intermediate + NH_3 \qquad (9)$$

with smearing parameters Δk = 0.005 Å^{-1} and ΔE = 0.025 eV. Subsequently, we added all Lorentzian functions, Intermediate $\xrightarrow{550\,°C}$ melamine + CO_2, and plot the results in Fig. 6. Note that the corresponding positions (relative to the reciprocal lattice vectors) of the high-symmetry points of the G PC, Γ_G, K_G and M_G in the SC Brillouin zone were calculated. As an example for K_G point, we have $K_G = k_{SC} \cdot P_G$. The new fractional positions of the symmetry points for the G monolayer are listed in Table 1. These theoretical results emulate the spin-resolved ARPES measurements of G/CrI$_3$ heterostructures. First, Dirac cones with majority-spin contributions are positioned above the Fermi energy at the K_G high-symmetry point. Several valence band discontinuities are observed for energy values less than −0.5 eV with the formation of spin-polarized minigaps. These spin-resolved minigaps, below −0.5 eV, were quantified and are shown in Fig. S4 of the SI. In general, these electronic minigaps have energy values larger than room temperature (25 meV). Therefore, the θ-dependence of the electronic structure of the G monolayer can be observed clearly around the K_G for two perpendicular directions in reciprocal space.

The formation of narrow single-spin polarized bands in G monolayer was achieved at θ = 30.0° and 23.4° above Fermi energy. Conversely, the two G/CrI$_3$ heterostructures with low θ exhibited parabolic bands near the Dirac point, as indicated by the blue arrows in Fig. 6. The electronic states with high spectral weights can be ascribed to the Dirac points of the G monolayer above the Fermi energy. These results are useful to determine the energy position of two Dirac points per spin and calculate a Zeeman-spin splitting energy, $\Delta_Z(\theta) = DP_\uparrow - DP_\downarrow$, with $DP_\uparrow$ ($DP_\downarrow$) denoting the energy position of majority-spin (minority-spin) Dirac point. The average results are $\Delta_Z(\theta)$ = +22, +24, +40 and −16 meV at θ = 30.0, 23.4, 12.5 and 4.1°, respectively. The positive Zeeman splitting could be correlated with an increase in the net magnetization of CrI$_3$, which could increase the effective magnetic field on the carbon atoms, favoring electron polarization in the carbon atoms of G along the direction of the net magnetization of CrI$_3$ (FM ordering in G). Note that pure FM ordering was observed at θ = 12.5°, where Zeeman splitting was at its maximum (see Fig. S2(c) of the SI). Conversely, the negative Zeeman splitting observed at θ = 4.1° increased the spin inversion, as shown in Fig. S2(d) of the SI. Thus, G exhibited small domains with AFM ordering. These outstanding results show twistable Zeeman-spin splitting with different values and signs. Finally, we clearly show the presence of magnetic minigaps in G, with different sizes and positions in energy, induced by the MPE of the CrI$_3$ monolayer with different orientations. Therefore, the interlayer rotation angle θ is an additional degree of freedom to control the magnetic moiré states in G due to the MPE with the FM semiconductor CrI$_3$ monolayer. It should be noted that external compression and electric fields, along with impurities, could be auxiliary knobs for tuning the electronic, magnetic, transport, topological and magnetoelectric properties,[10,12,13,47] which deserves further study.
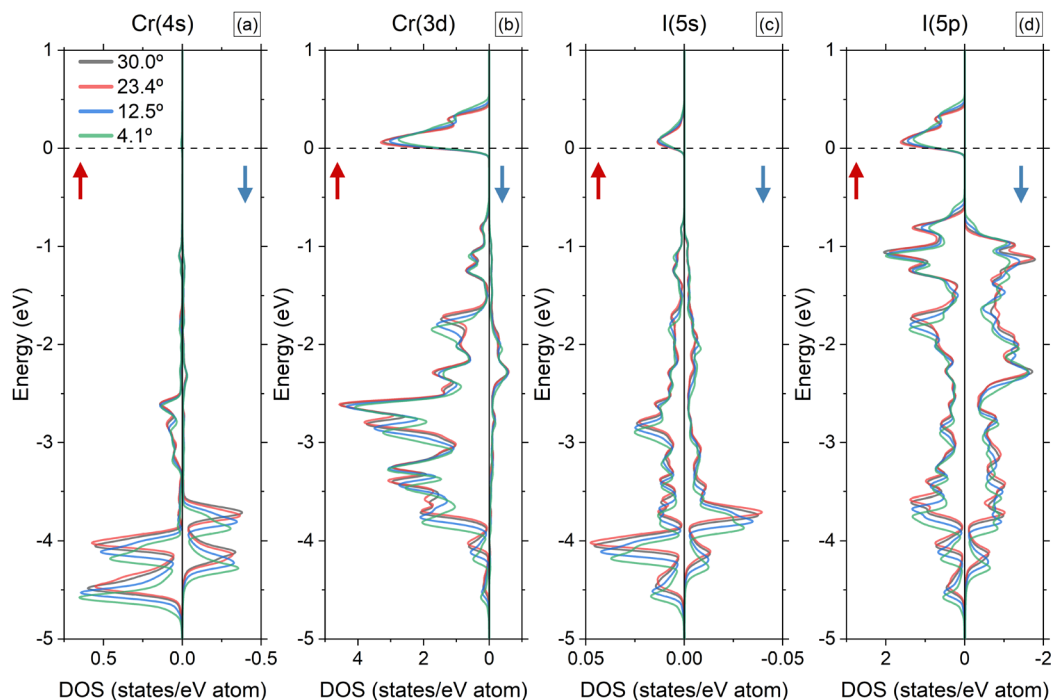

Fig. 7 Average atom- and orbital-resolved density of states (DOS) for I and Cr atoms: (a) Cr(4s), (b) Cr(3d), (c) I(5s), and (d) I(5p) states. Red (blue) arrows denote majority-spin (minority-spin) contributions. The Fermi energy is set to 0 eV.

3.6 Atom and orbital contributions of CrI$_3$

Fig. 7 presents the angle-dependent average atom- and orbital-resolved DOS of CrI$_3$ based on the spin contribution. The FM state in CrI$_3$ leads to an asymmetric energy behavior between the occupied majority-spin and minority-spin states from −5 to 0 eV. A downshift in the energy trend is observed as θ decreases. Less dispersive Cr(4s) states are positioned between −3.5 and −5 eV, and they do not contribute at the Fermi level. In the same valence regime, the Cr(4s) states were mixed with those of I(5s) and I(5p) orbitals. On the other hand, the mixing of Cr(3d) and mainly I(5p) orbitals extends from −4 eV to the Fermi energy. Notably, only the majority-spin Cr(3d) states contribute to this energy regime, and the minority-spin I(5p) orbitals generally prevail in the valence regime. Also, a majority-spin admixture of Cr(3d), I(5p), and I(5s) orbitals spans from the Fermi energy up to 0.5 eV, with the Cr(3d) and I(5p) orbitals predominating.

A more detailed analysis of the orbital-resolved DOS for the I(5p) orbitals per up (near to G) and down (far from G) layers is shown in Fig. 8. The iodine top (I$_T$) and bottom (I$_B$) layer represent the I orbital states that are closer to and farthest from the G monolayer. The perpendicular and degenerate in-plane electronic I states were attributed to I(5p$_z$) and I(5p$_{x,y}$), respectively. In general, an increase in the bandwidth is obtained as the θ tends toward low values with attenuation for the majority-spin I(5p$_z$) states close to the Fermi energy. The I(5p$_{x,y}$) in-plane states broaden more than I(5p$_z$) to deeper energies because of bonding with I(4s) orbitals, as shown in Fig. 7.

3.7 Magnetic exchange coupling

In addition to the novel and twistable electronic and magnetic properties of G induced by the MPE of the CrI$_3$ monolayer, this section presents the results of the adjustable exchange coupling parameter J between the Cr spins due to the interfacial effect of the G monolayer. To obtain the J value, we first performed DFT calculations for two different magnetic configurations, a ferromagnetic (FM) state and another Néel antiferromagnetic (AFM) state (see Fig. S5 of the SI for more details) to obtain the corresponding total energy; and with these energy values, we then solve the next classical Heisenberg spin Hamiltonian:

$$\text{Melamine} \xrightarrow{550\,°C} \text{g-C}_3\text{N}_4 + 8\text{NH}_3 \tag{10}$$
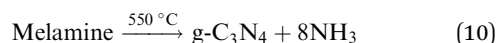
where E_0 is the total energy of the non-magnetic ground state, $J_{i,j}$ is the exchange coupling term between the nearest-neighbor i and j sites, and S_i (S_j) is the spin vector for each i (j) Cr atom. Because we found an overestimated local magnetic moment of the Cr atom in Table SIII of the SI, we adopt the $\sim 3.0\mu_B$[44] value leading to a Cr atom with +3e charge and spin $|S_i| = 3/2$. The total energy results for G/CrI$_3$ systems show that the FM configuration is more stable than the Néel AFM configuration, with the energy difference $\Delta E_{\text{FM–AFM}} = E_{\text{FM}} - F_{\text{AFM}}$ values reported in Table 1. Compared with the bare CrI$_3$ monolayer with $\Delta E_{\text{FM–AFM}} = -64$ meV per unit cell, we found that the energy difference between the two magnetic configurations (FM and Néel-AFM) was lower and favored perpendicular FM alignment to the G/CrI$_3$ heterostructure. The corresponding expression for the magnetic exchange interaction per Cr atom
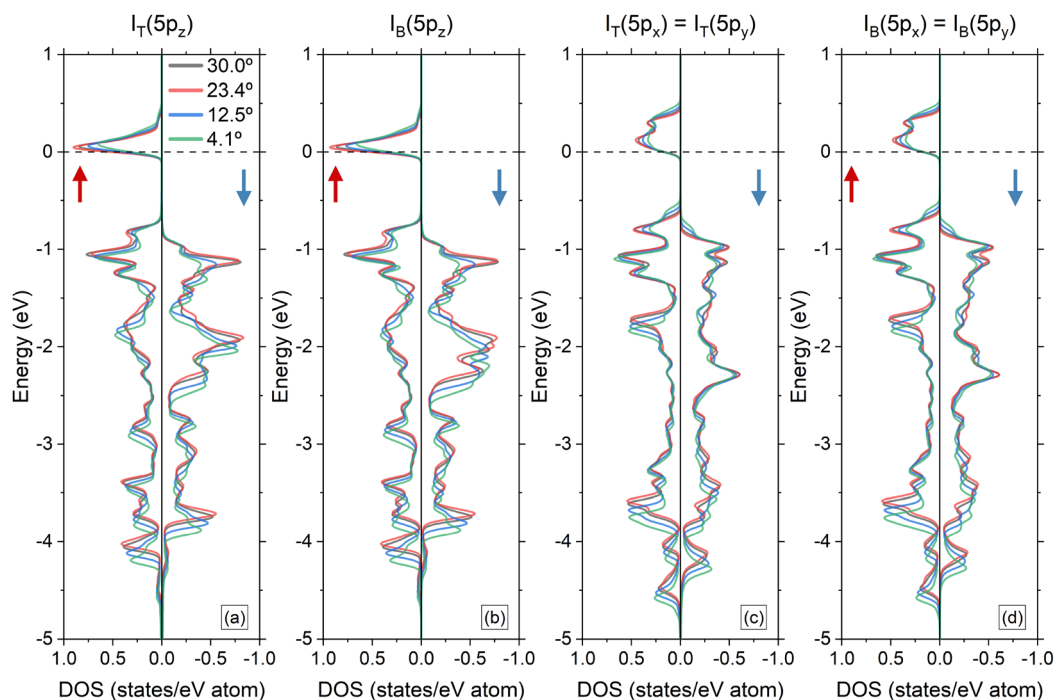

Fig. 8 Average orbital-resolved density of states (DOS) for I atoms: (a) I$_T$(5p$_z$), (b) I$_B$(5p$_z$), (c) I$_T$(5p$_x$) = I$_T$(5p$_y$), and (d) I$_B$(5p$_x$) = I$_B$(5p$_y$). The subscript T (B) labels the orbital contributions from I atoms nearer (farther) to the G monolayer. Red (blue) arrows denote majority–spin (minority–spin) contributions. The Fermi energy is set to 0 eV.

is $J = \Delta E_{FM-AFM}/12|S|^2$ and the calculated values are shown in Table 1. First, all the J values are negative which means that the intralayer nearest-neighbor Cr–Cr coupling is FM, and indeed the J values for twisted G/CrI$_3$ heterostructures are lower than the calculated value of $J = -2.37$ meV/Cr for the pristine CrI$_3$ layer. Our calculated value $J = -2.37$ meV/Cr is in reasonable agreement with other reports.[14,44,48–51] From this analysis, we expect that the Curie temperature $T_C = 45$ K of the CrI$_3$ monolayer[4,52] will increase as in the 2D vdW CrPS$_4$ magnet by the MPE owing to the monolayer G;[53] but also, it will be twist-angle programmable.

4 Conclusions

In summary, we presented a detailed and systematic study of the building of periodic graphene/CrI$_3$ heterostructures and then calculated the ground state structural, electronic, and magnetic properties using collinear spin-polarized DFT calculations. Four twisted heterostructures were built with maximal biaxial strain to avoid renormalization of the band structures and possible expansion, shrinkage, or corrugation of the graphene monolayer. Once the geometry was optimized, we found the same electronic bandwidth in graphene with a magnetic effect induced by ferromagnetic and semiconducting monolayers. Specifically, the maximum stress produces a reduction in the magnitude of the magnetic moments of carbon and favors spin reversal, giving rise to local AFM ordering in graphene. Clear fingerprints of the moiré effects are observed in the local spin density, spin-polarization ratio, orbital-resolved density of states and unfolded band structures for graphene, and an enhancement in the magnetic exchange coupling is observed in the CrI$_3$ monolayer. Therefore, the interlayer rotation angle is an additional degree of freedom for the compression and electric fields to program the magnetic states in the vdW graphene/CrI$_3$ heterostructures.

Author contributions

F. L. U. and F. S. O. contributed to conceptualization, formal analysis, investigation, methodology, supervision, validation, visualization, and writing – original draft.

Conflicts of interest

There are no conflicts to declare.

Data availability

The data supporting this article have been included as part of the supplementary information (SI). Supplementary information: tables with structural information (Table SI), atomic charges (Table SII) and magnetic moments (Table SIII); electronic properties of pristine graphene layer (Fig. S1); 2D maps of Mulliken atomic charges in graphene (Fig. S2) and resulting magnetic moments (Fig. S3); spin-resolved unfolded band structures with minigap values (Fig. S4); and top and side views of magnetic configurations in the CrI$_3$ layer (Fig. S5). See DOI: https://doi.org/10.1039/d5tc03721b.

References

1 K. S. Novoselov, A. K. Geim, S. V. Morozov, D.-E. Jiang, Y. Zhang, S. V. Dubonos, I. V. Grigorieva and A. A. Firsov, *Science*, 2004, **306**, 666–669.

2 I. Z. Žutić, J. Fabian and S. Das Sarma, *Rev. Mod. Phys.*, 2004, **76**, 323–410.

3 A. Hirohata, K. Yamada, Y. Nakatani, I.-L. Prejbeanu, B. Diény, P. Pirro and B. Hillebrands, *J. Magn. Magn. Mater.*, 2020, **509**, 166711.

4 B. Huang, G. Clark, E. Navarro-Moratalla, D. R. Klein, R. Cheng, K. L. Seyler, D. Zhong, E. Schmidgall, M. A. McGuire and D. H. Cobden, *et al.*, *Nature*, 2017, **546**, 270–273.

5 E. C. Ahn, *npj 2D Mater. Appl.*, 2020, **4**, 17.

6 Y. Liu, C. Zeng, J. Zhong, J. Ding, Z. M. Wang and Z. Liu, *Nano-Micro Lett.*, 2020, **12**, 1–26.

7 C.-Z. Chang, W. Zhao, D. Y. Kim, H. Zhang, B. A. Assaf, D. Heiman, S.-C. Zhang, C. Liu, M. H. Chan and J. S. Moodera, *Nat. Mater.*, 2015, **14**, 473–477.

8 J. Jeong, D. H. Kiem, D. Guo, R. Duan, K. Watanabe, T. Taniguchi, Z. Liu, M. J. Han, S. Zheng and H. Yang, *Adv. Mater.*, 2024, **36**, 2310291.

9 C. Cardoso, D. Soriano, N. A. García-Martínez and J. Fernández-Rossier, *Phys. Rev. Lett.*, 2018, **121**, 067701.

10 M. U. Farooq and J. Hong, *npj 2D Mater. Appl.*, 2019, **3**, 3.

11 I. Rozhansky and V. Fal'ko, *Phys. Rev. Mater.*, 2024, **8**, 074007.

12 J. Zhang, B. Zhao, T. Zhou, Y. Xue, C. Ma and Z. Yang, *Phys. Rev. B*, 2018, **97**, 085401.

13 J.-T. Ren, Y. Feng, S.-S. Ke and H.-F. Lü, *Adv. Phys. Res.*, 2025, **4**, 2300026.

14 S. Bandyopadhyay, F. L. Buessen, R. Das, F. G. Utermohlen, N. Trivedi, A. Paramekanti and I. Dasgupta, *Phys. Rev. B*, 2022, **105**, 184430.

15 Z. Qiu, M. Holwill, T. Olsen, P. Lyu, J. Li, H. Fang, H. Yang, M. Kashchenko, K. S. Novoselov and J. Lu, *Nat. Commun.*, 2021, **12**, 70.

16 C.-C. Tseng, T. Song, Q. Jiang, Z. Lin, C. Wang, J. Suh, K. Watanabe, T. Taniguchi, M. A. McGuire and D. Xiao, *et al.*, *Nano Lett.*, 2022, **22**, 8495–8501.

17 K. Zollner and J. Fabian, *Phys. Rev. Lett.*, 2022, **128**, 106401.

18 C. Tang, Z. Zhang, S. Lai, Q. Tan and W.-B. Gao, *Adv. Mater.*, 2020, **32**, 1908498.

19 S. K. Behera, M. Bora, S. S. P. Chowdhury and P. Deb, *Phys. Chem. Chem. Phys.*, 2019, **21**, 25788–25796.

20 J. Zhang, B. Paulus, Y. Dedkov and E. Voloshina, *J. Mater. Chem. C*, 2025, **13**, 11789–11799.

21 M. Jugovac, I. Cojocariu, J. Sánchez-Barriga, P. Gargiani, M. Valvidares, V. Feyer, S. Blügel, G. Bihlmayer and P. Perna, *Adv. Mater.*, 2023, **35**, 2301441.

22 A. M. Holmes, S. Pakniyat, S. A. H. Gangaraj, F. Monticone, M. Weinert and G. W. Hanson, *Phys. Rev. B*, 2020, **102**, 075435.

23 T. Naimer, K. Zollner, M. Gmitra and J. Fabian, *Phys. Rev. B*, 2021, **104**, 195156.

24 N. Troullier and J. L. Martins, *Phys. Rev. B*, 1991, **43**, 1993.

25 P. Ordejón, E. Artacho and J. M. Soler, *Phys. Rev. B*, 1996, **53**, R10441.

26 J. M. Soler, E. Artacho, J. D. Gale, A. Garca, J. Junquera, P. Ordejón and D. Sánchez-Portal, *J. Phys.: Condens. Matter*, 2002, **14**, 2745.

27 R. Cuadrado and J. I. Cerdá, *J. Phys.: Condens. Matter*, 2012, **24**, 086005.

28 O. A. Vydrov and T. van Voorhis, *J. Chem. Phys.*, 2010, **133**, 244103.

29 S. L. Dudarev, G. A. Botton, S. Y. Savrasov, C. J. Humphreys and A. P. Sutton, *Phys. Rev. B*, 1998, **57**, 1505–1509.

30 F. Haddadi, E. Linscott, I. Timrov, N. Marzari and M. Gibertini, *Phys. Rev. Mater.*, 2024, **8**, 014007.

31 I. V. Kashin, V. V. Mazurenko, M. I. Katsnelson and A. N. Rudenko, *2D Mater.*, 2020, **7**, 025036.

32 Y. S. Hou, J. W. Kim and R. Q. Wu, *Phys. Rev. B*, 2020, **101**, 121401.

33 V. Kumar Gudelli and G.-Y. Guo, *New J. Phys.*, 2019, **21**, 053012.

34 H. J. Monkhorst and J. D. Pack, *Phys. Rev. B*, 1976, **13**, 5188–5192.

35 L. Bengtsson, *Phys. Rev. B*, 1999, **59**, 12301–12304.

36 K. Momma and F. Izumi, *J. Appl. Crystallogr.*, 2011, **44**, 1272–1276.

37 Y. Betancur-Ocampo, S. Galván Y García, S. Tehuacanero-Nuñez, J. Reyes-Gasga, T. Stegmann and F. Sánchez-Ochoa, *Phys. Rev. B*, 2025, **111**, 085431.

38 F. Sánchez-Ochoa, A. R. Botello-Méndez and C. Noguez, *Phys. Rev. B*, 2021, **104**, 075430.

39 C. Cardoso, A. T. Costa, A. H. MacDonald and J. Fernández-Rossier, *Phys. Rev. B*, 2023, **108**, 184423.

40 O. Aguilar-Espíndola, OssielAg/Nook-iin: Nook'iin: First public version, 2024, https://doi.org/10.5281/zenodo.14257397.

41 F. Hidalgo, F. Sánchez-Ochoa and C. Noguez, *npj 2D Mater. Appl.*, 2023, **7**, 40.

42 F. Sánchez-Ochoa, F. Hidalgo, M. Pruneda and C. Noguez, *J. Phys.: Condens. Matter*, 2020, **32**, 025501.

43 O. Aguilar-Spíndola, A. Rubio-Ponce, F. López-Urías and F. Sánchez-Ochoa, *Phys. Chem. Chem. Phys.*, 2025, **27**, 11541–11550.

44 Q. Yang, X. Hu, X. Shen, A. V. Krasheninnikov, Z. Chen and L. Sun, *ACS Appl. Mater. Interfaces*, 2021, **13**, 21593–21601.

45 F. Sánchez-Ochoa, *Phys. Rev. Appl.*, 2022, **18**, 054068.

46 S. G. y García, Y. Betancur-Ocampo, F. Sánchez-Ochoa and T. Stegmann, *Nano Lett.*, 2024, **24**, 2322–2327.

47 X.-Q. Tian, A. Hassan, Y. Wang, Q.-F. Sun, X.-R. Wang, T. Altalhi, Y. Du and B. I. Yakobson, *Adv. Funct. Mater.*, 2025, 2503185.

48 W.-B. Zhang, Q. Qu, P. Zhu and C.-H. Lam, *J. Mater. Chem. C*, 2015, **3**, 12457–12468.

49 H. Wang, F. Fan, S. Zhu and H. Wu, *Europhys. Lett.*, 2016, **114**, 47001.

50 L. Chen, J.-H. Chung, T. Chen, C. Duan, A. Schneidewind, I. Radelytskyi, D. J. Voneshen, R. A. Ewings, M. B. Stone, A. I. Kolesnikov, B. Winn, S. Chi, R. A. Mole, D. H. Yu, B. Gao and P. Dai, *Phys. Rev. B*, 2020, **101**, 134418.

51 W. Su, D. Wang, D. Wei and Z. Dai, *Metals*, 2025, **15**, 398.

52 K. L. Seyler, D. Zhong, D. R. Klein, S. Gao, X. Zhang, B. Huang, E. Navarro-Moratalla, L. Yang, D. H. Cobden and M. A. McGuire, *et al.*, *Nat. Phys.*, 2018, **14**, 277–281.

53 W. Zhu, C. Song, L. Han, H. Bai, C. Chen and F. Pan, *Phys. Rev. B*, 2023, **108**, L100406.